Supporting Information

Probing the electronic and ionic transports in topologically distinct redox-active metal–organic frameworks in aqueous electrolytes

Cheng-Hui Shen,[a] Yu-Hsiu Chen,[a] Yi-Ching Wang,[a] Tzu-En Chang,[a] You-Liang Chen,[a] and Chung-Wei Kung *[a]

[a] Department of Chemical Engineering, National Cheng Kung University, Tainan City, Taiwan, 70101.

*Email: cwkung@mail.ncku.edu.tw

NMR experiments were conducted to examine the presence of benzoate coordinated on the hexa-zirconium nodes of CAU-24, and NMR spectra of the digested CAU-24 samples in D_2SO_4/ DMSO-d_6 solutions are shown in Figure S1. For comparison, the CAU-24 sample prepared without performing the heating step in the HCl/DMF mixture was also collected and subjected to NMR measurement. From the ratio of the integrated areas for the peaks of TCPB linkers to those of benzoic acid, there are on average 1.52 benzoates per linker and, therefore 3.04 benzoates coordinated on per hexa-zirconium node when the HCl/DMF process is not used. NMR peaks of benzoates cannot be observed in the spectrum of the digested CAU-24 after performing the HCl/DMF heating process, indicating that benzoates can be totally removed by such an activation step. Besides, more coordinated formate generated by the thermal decomposition of DMF can also be observed in the HCl/DMF-activated CAU-24, with the loading of 0.38 per node. Thus, the molecular formula of CAU-24 synthesized here after activation was determined as $Zr_6(\mu_3\text{-}O)_4(\mu_3\text{-}OH)_4(TCPB)_2(HCOO)_{0.38}(OH)_{3.62}(OH_2)_{3.62}$.

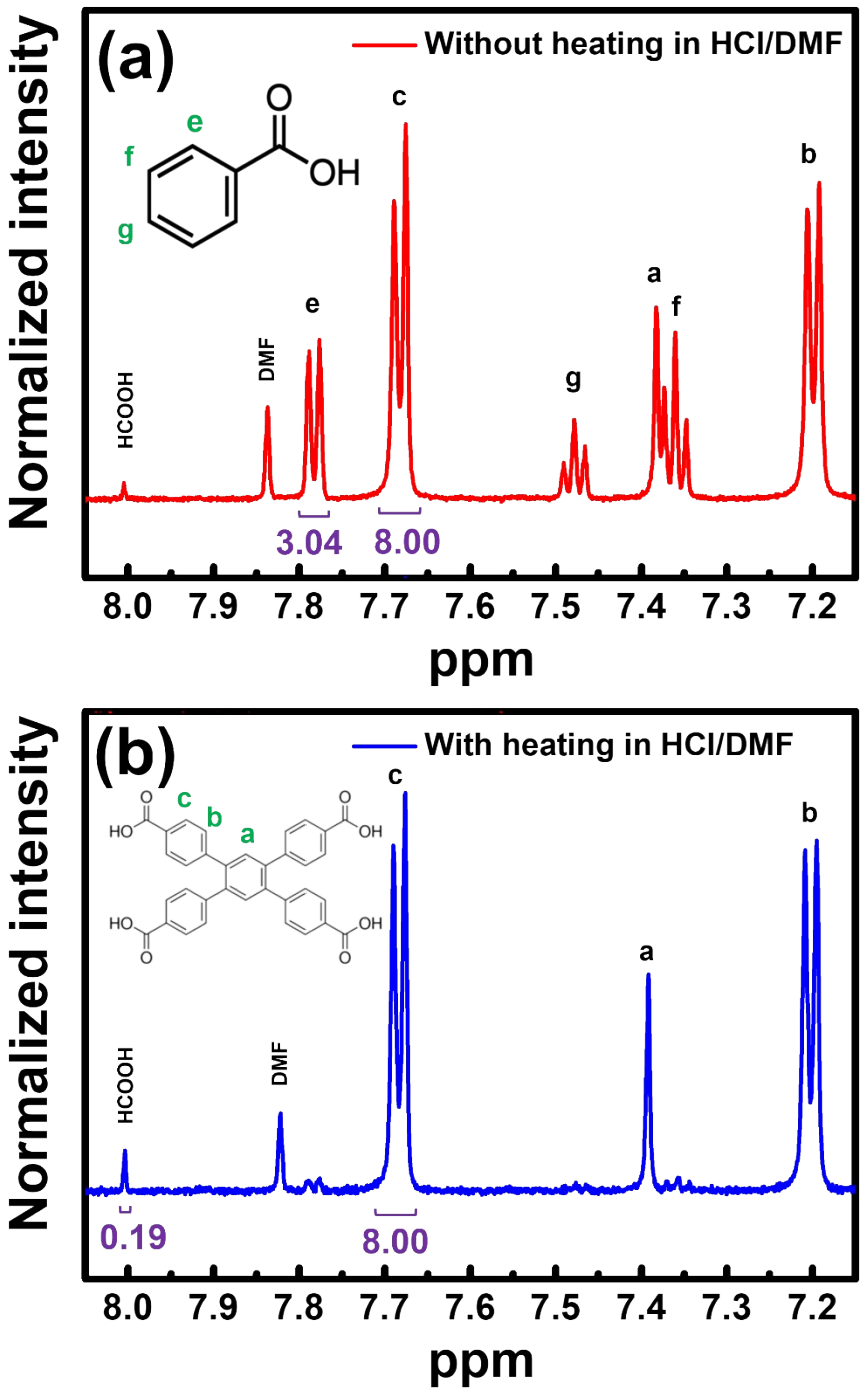

Figure S1. ^{1}H NMR spectra of the digested CAU-24 synthesized (a) without performing the HCl/DMF heating process and (b) with the HCl/DMF heating process.

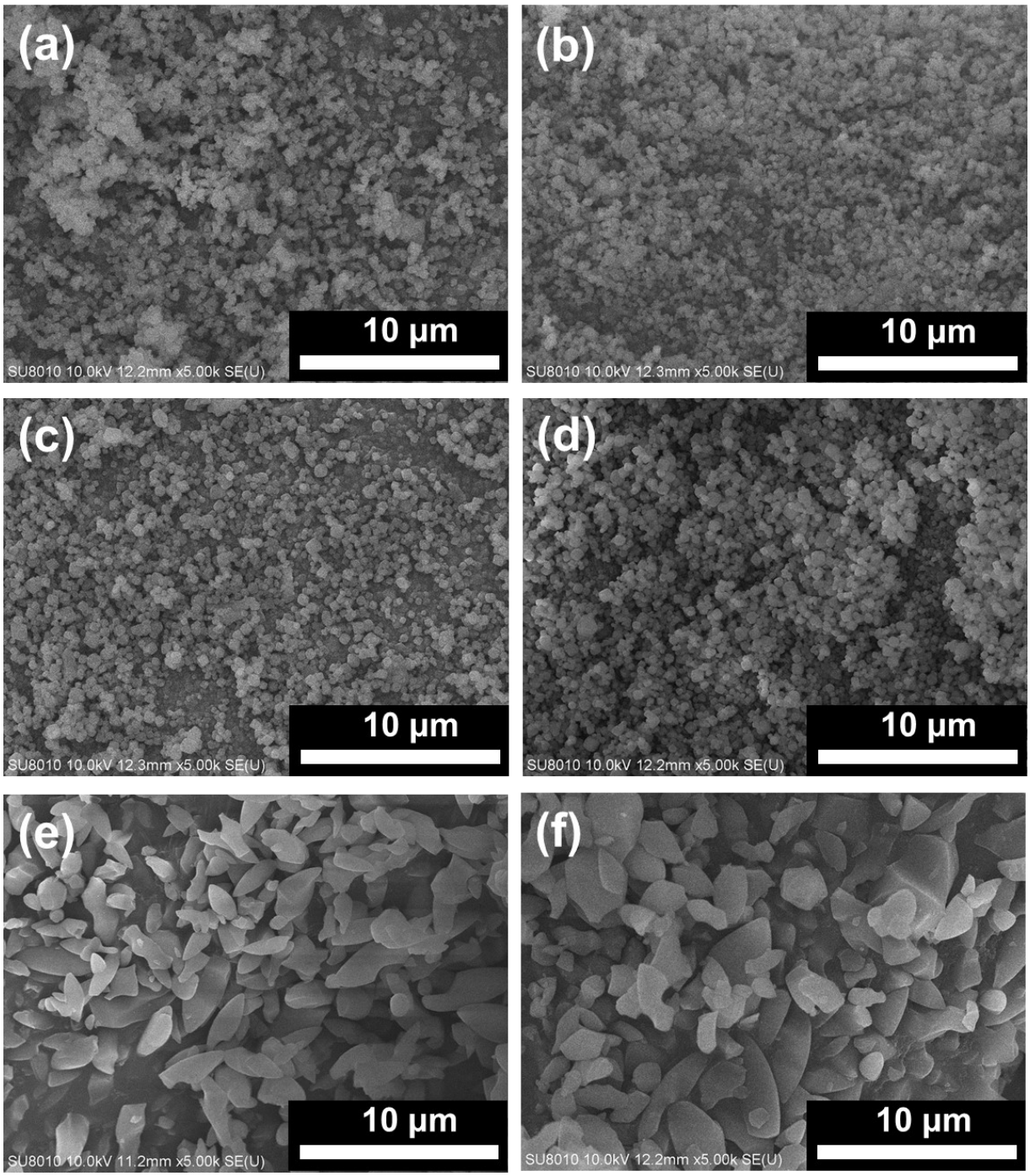

Figure S2. Low-magnification SEM images of (a) MOF-808, (b) Mn-MOF-808, (c) UiO-66, (d) Mn-UiO-66, (e) CAU-24, and (f) Mn-CAU-24.

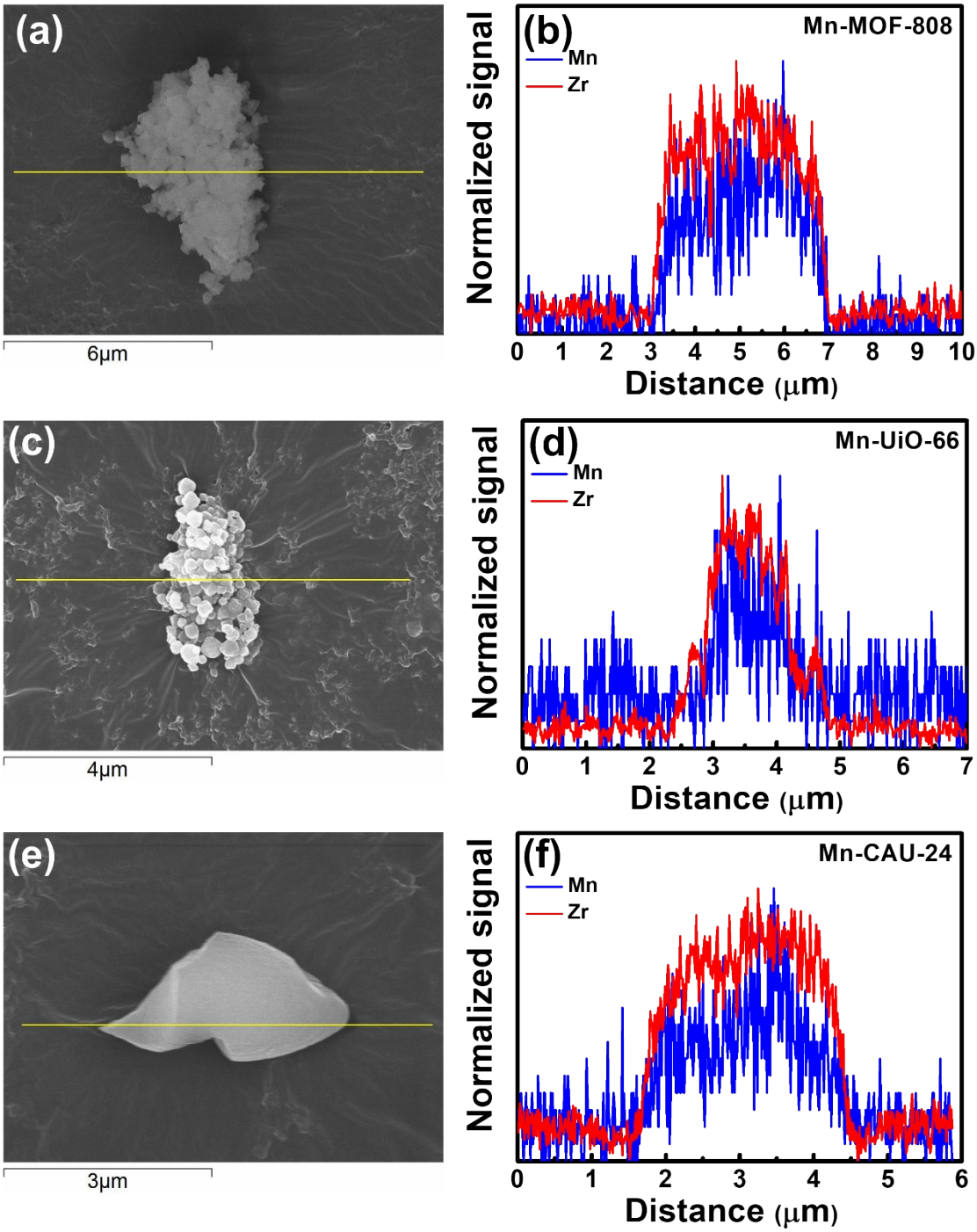

Figure S3. SEM images of (a) Mn-MOF-808, (c) Mn-UiO-66, and (e) Mn-CAU-24. Spatial distributions of Mn and Zr in (b) Mn-MOF-808, (d) Mn-UiO-66, and (f) Mn-CAU-24, obtained by utilizing EDS line scan on the yellow lines shown in (a), (c), and (e), respectively.

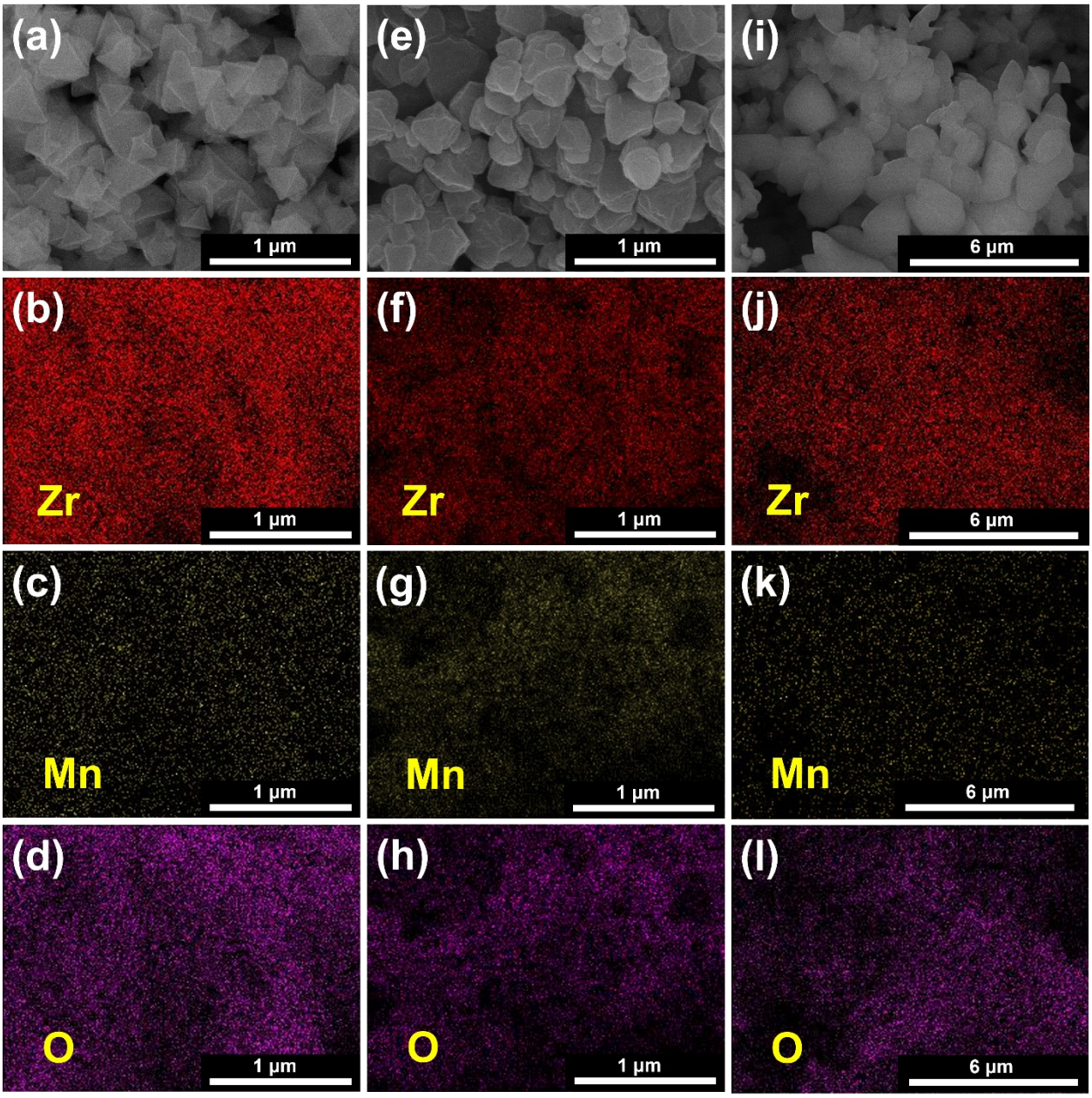

Figure S4. (a) SEM image of Mn-MOF-808 and (b-d) the corresponding EDS mapping images. (e) SEM image of Mn-UiO-66 and (f-h) the corresponding EDS mapping images. (i) SEM image of Mn-CAU-24 and (j-l) the corresponding EDS mapping images.

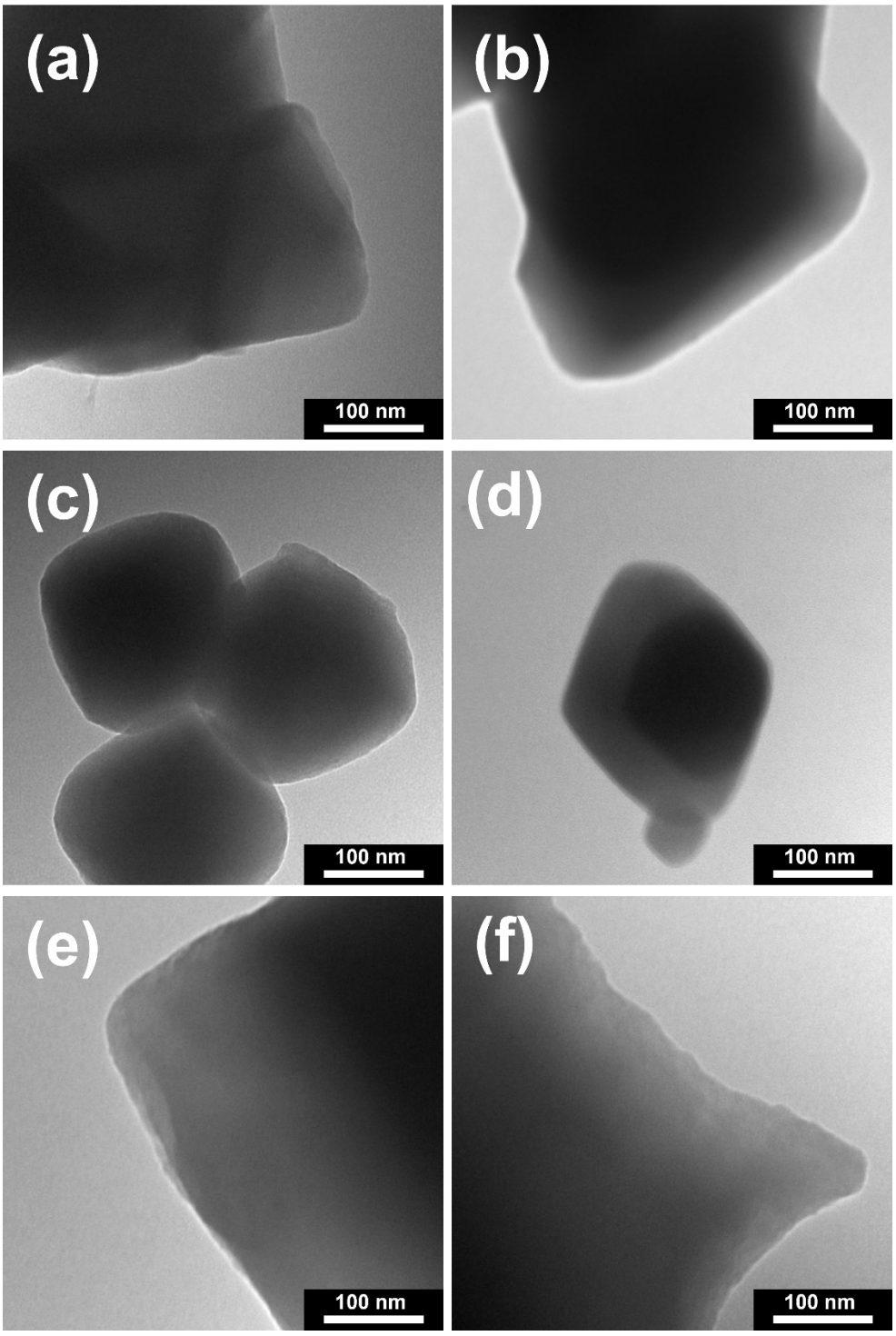

Figure S5. TEM images of (a) MOF-808, (b) Mn-MOF-808, (c) UiO-66, (d) Mn-UiO-66, (e) CAU-24, and (f) Mn-CAU-24.

FTIR spectra of all the three Zr-MOFs and their Mn-decorated materials are shown in Figure S6. The FTIR spectrum of MOF-808 shows peaks located at 1,381 cm^{-1}, 1,445 cm^{-1}, 1,568 cm^{-1}, and 1,658 cm^{-1}, which correspond to the symmetric vibration of O-C-O, the vibration of C=C in the aromatic ring of the BTC linker, the asymmetric vibration of O-C-O, and the stretching vibration of C=O originated from the residual DMF, respectively;[1-3] these FTIR characteristics are in general consistent with those reported for MOF-808 in literature.[1] For Mn-MOF-808, its FTIR spectrum is almost the same as that of MOF-808. For UiO-66, the similar four FTIR responses for the symmetric vibration of O-C-O, C=C in the aromatic ring of the linker, asymmetric vibration of O-C-O, and stretching vibration of C=O can also be observed in its spectrum, but the first three peaks shift to 1,400 cm^{-1}, 1,506 cm^{-1}, and 1,580 cm^{-1}, respectively. Such peak locations also agree well with those reported in the FTIR spectrum of UiO-66.[2] The FTIR spectrum does not change after the installation of manganese for UiO-66 as well. In the FTIR spectrum of CAU-24, these peaks for the symmetric vibration of O-C-O, C=C in the aromatic ring of the linker, asymmetric vibration of O-C-O, and stretching vibration of C=O can also be observed at 1,413 cm^{-1}, 1,545 cm^{-1}, 1,603 cm^{-1}, and 1,658 cm^{-1}, respectively. These peak locations are also consistent with those reported for CAU-24 in previous work,[3] and a similar spectrum was also obtained for Mn-CAU-24. Findings here indicate that the installation of Mn sites in all the three Zr-MOFs does not significantly change the structures of their organic moieties.

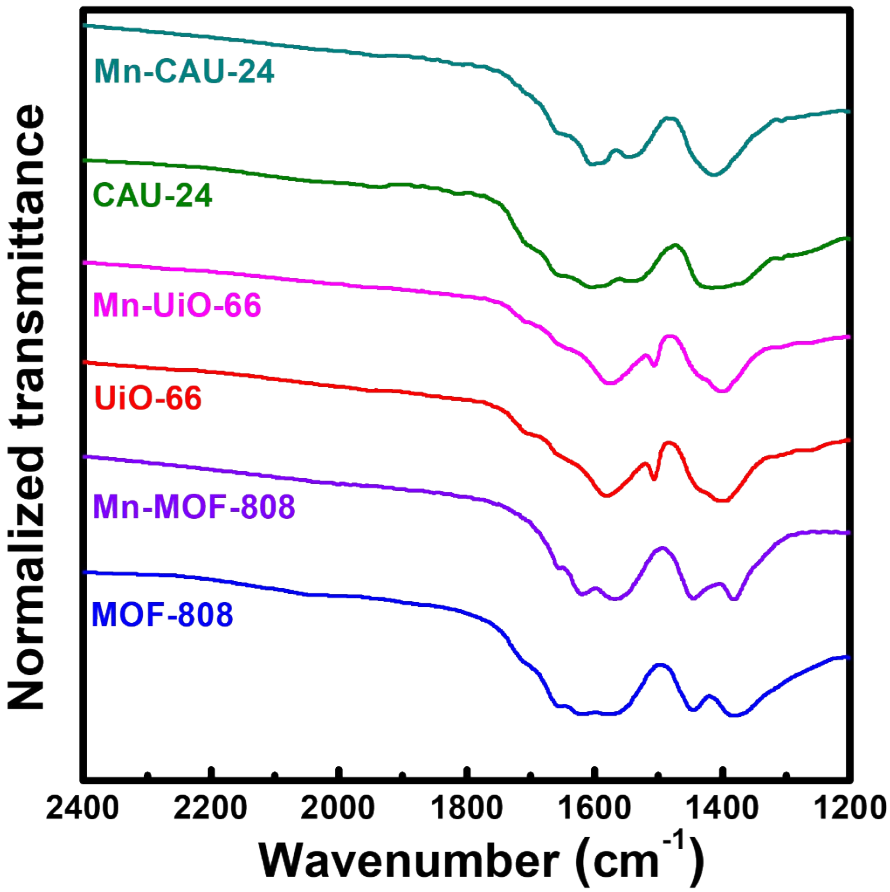

Figure S6. FTIR spectra of MOF-808, Mn-MOF-808, UiO-66, Mn-UiO-66, CAU-24, and Mn-CAU-24.

Raman spectra of all the three Zr-MOFs and their Mn-decorated materials are shown in Figure S7. The spectra of all the six materials show quite similar characteristics, with three main peaks located at around 580 cm^{-1}, 800 cm^{-1}, and 1,100 cm^{-1}. These peaks come from the C-C-C in plane bending, O-H bending and/or C-C symmetric breathing, and C-C symmetric ring breathing, respectively.[4] Another significant peak located at 1,615 cm^{-1} can be found in the spectra of CAU-24-based materials, but this peak becomes much smaller and barely observable in the spectra of UiO-66-based materials and MOF-808-based materials, respectively. According to the literature,

this peak should correspond to the C-C aromatic stretch in phase present in the organic linkers of Zr-MOFs.[4] This peak shows a fairly strong intensity in the spectra of CAU-24-based materials since the TCPB linker possesses the highest number of aromatic rings compared to BDC and BTC. In general, the four characteristic peaks present in the Raman spectra of all the six materials reported here agree well with those present in the Raman spectra of Zr-MOFs reported previously.[4]

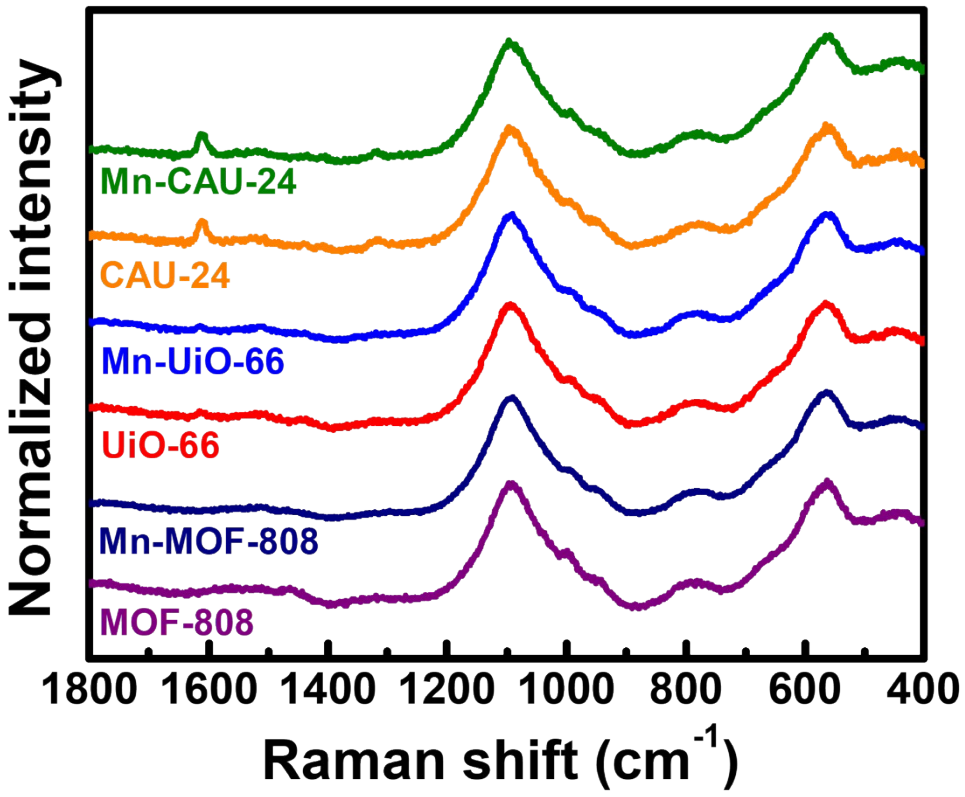

Figure S7. Raman spectra of MOF-808, Mn-MOF-808, UiO-66, Mn-UiO-66, CAU-24, and Mn-CAU-24.

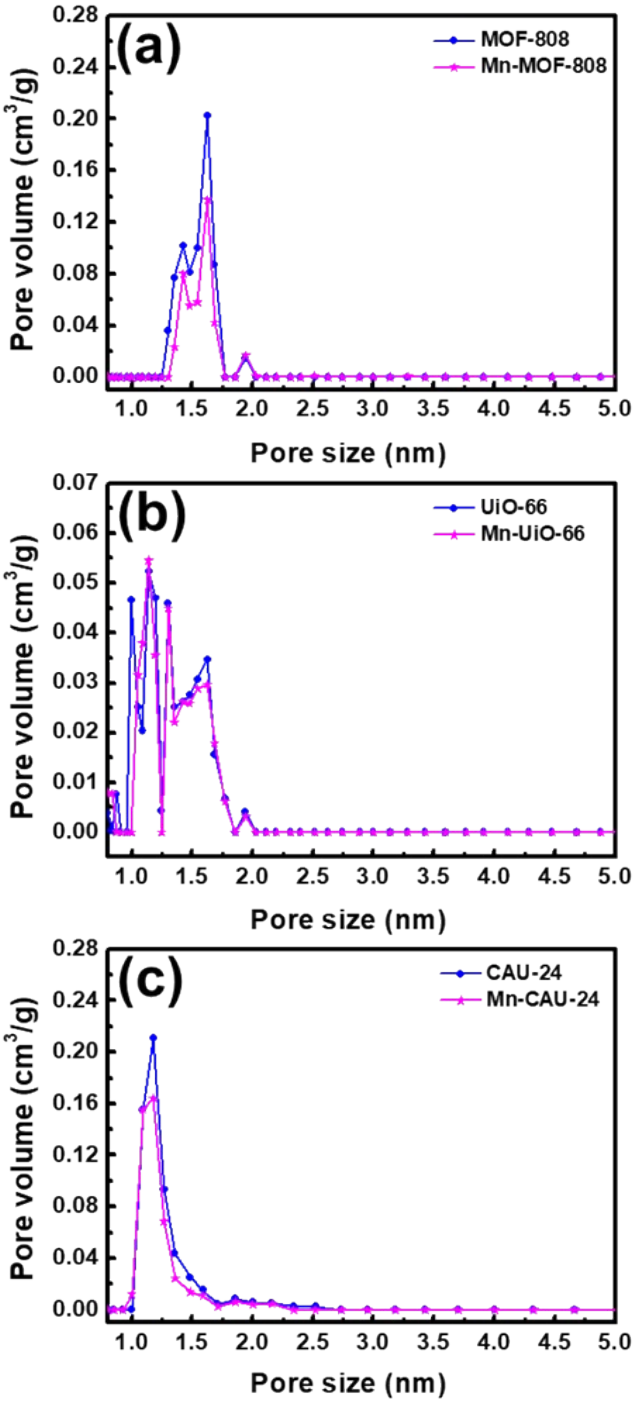

Figure S8. DFT pore size distributions of (a) MOF-808 and Mn-MOF-808, (b) UiO-66 and Mn-UiO-66, and (c) CAU-24 and Mn-CAU-24. All pore size distributions were calculated from the isotherms shown in Figure 4 in the main text by using the NLDFT model.

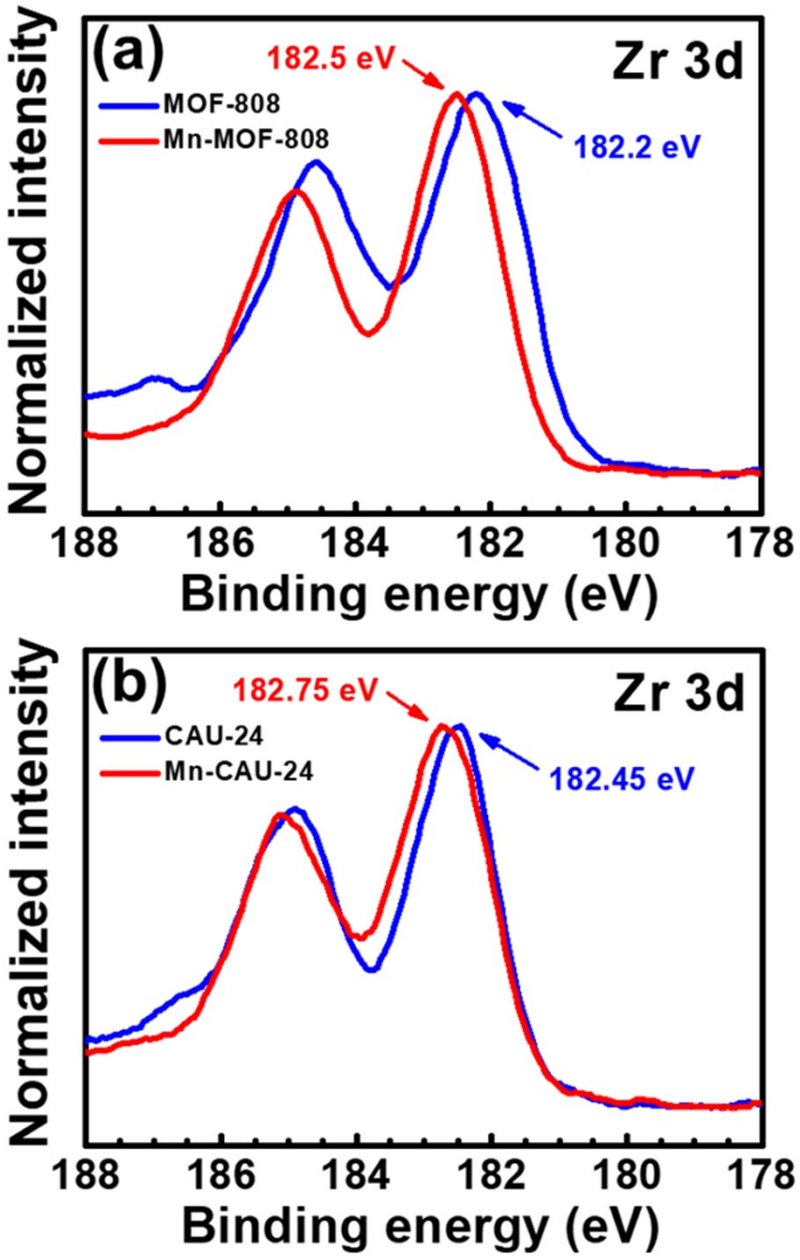

Figure S9. XPS spectra of (a) MOF-808 and Mn-MOF-808, and (b) CAU-24 and Mn-CAU-24 in the Zr 3d region.

To measure the bulk electrical conductivity (σ) of each Mn-decorated Zr-MOF, the dry pellets of these materials were subjected to two-probe cyclic voltammetric measurements, and the σ was calculated by the following equation,

$$\sigma = \frac{l}{RA}$$

where R is the electrical resistance estimated from the slope of the cyclic voltammetric curve near 0 V shown in Figure S10, l is the thickness of the pellet, and A is the cross-section area of the pellet. As shown in Figure S10, all pellets of the three Mn-decorated Zr-MOFs only show the current response below the scale of 1 nA with huge noises, and the slope can only be obtained by linearly fitting the noisy data. The obtained σ of Mn-decorated Zr-MOFs are listed in Table S1.

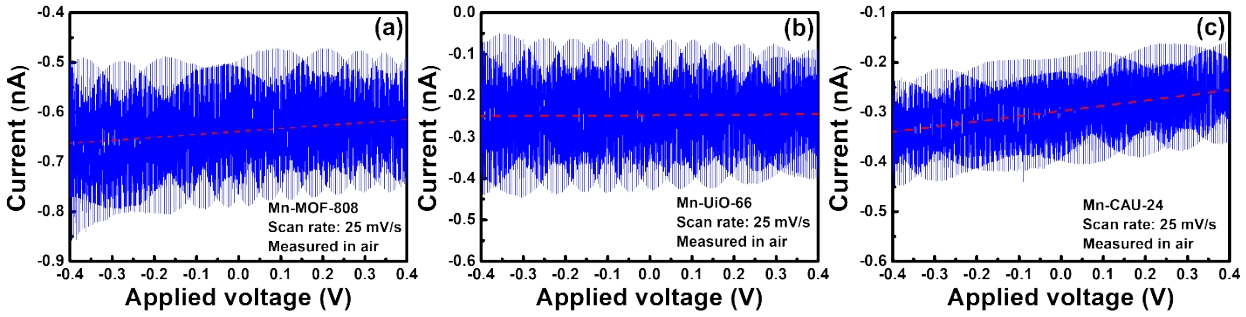

Figure S10. Cyclic voltammetric curves of the pellets of (a) Mn-MOF-808, (b) Mn-UiO-66, and (c) Mn-CAU-24. The dash line indicates the fitting curve of the data for estimating the σ.

Table S1. Results calculated from the data shown in Figure S10.

	R (Ω)	l (cm)	A (cm^2)	σ (S/cm)
Mn-MOF-808	1.68×10^{10}	0.018	0.3848	2.78×10^{-12}
Mn-UiO-66	1.56×10^{11}	0.026	0.3848	4.33×10^{-13}
Mn-CAU-24	9.48×10^{9}	0.021	0.3848	5.76×10^{-12}

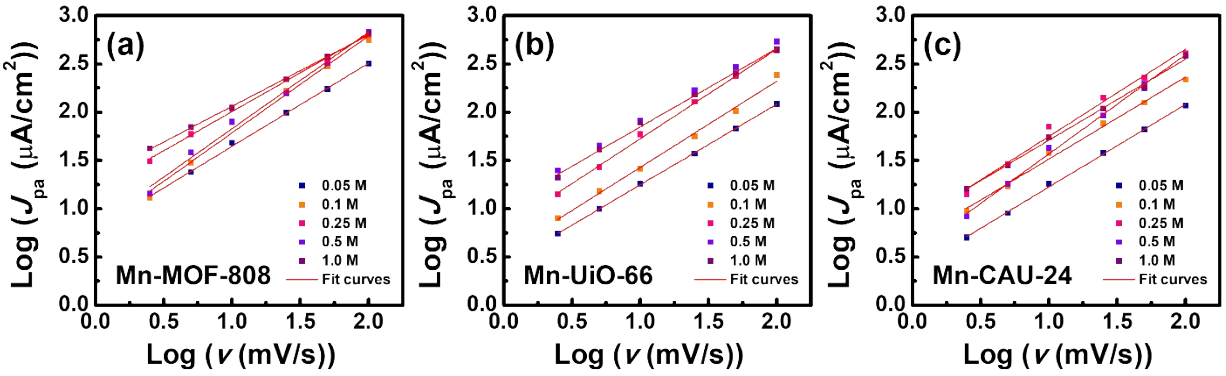

Figure S11. Plots of log(J_{pa}) vs. log(v) extracted from Figure 5-7 in the main text.

Table S2. Slopes obtained from the fitting curves shown in Figure S11.

Thin film / Concentration of electrolyte	0.05 M	0.1 M	0.25 M	0.5 M	1.0 M
Mn-MOF-808	0.86	1.00	0.81	1.00	0.74
Mn-UiO-66	0.84	0.88	0.93	0.83	0.81
Mn-CAU-24	0.86	0.85	0.90	1.03	0.84

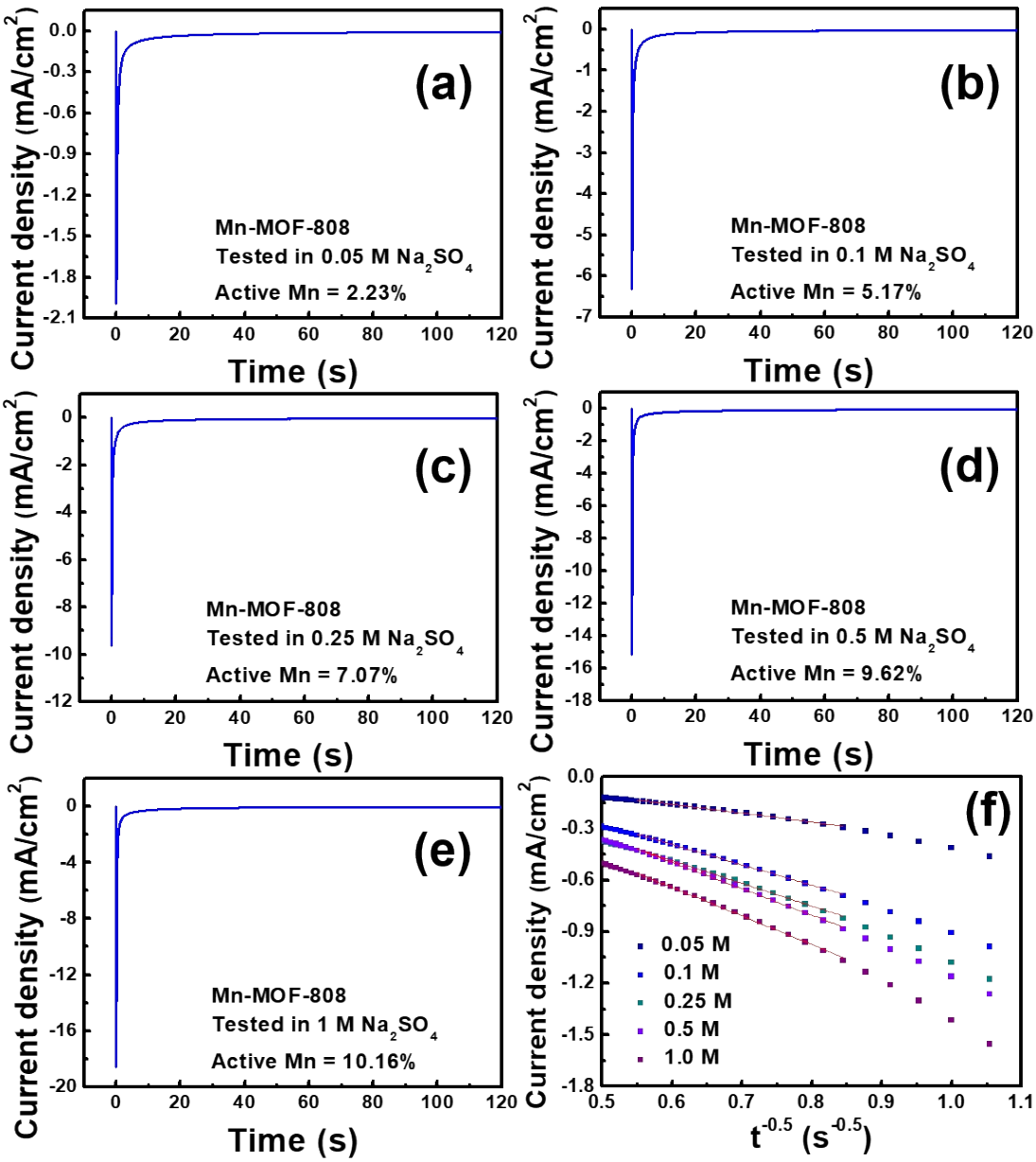

Figure S12. Chronoamperometric curves of Mn-MOF-808 thin films measured in (a) 0.05 M, (b) 0.1 M, (c) 0.25 M, (d) 0.5 M, and (e) 1 M Na_2SO_4 (aq). Each thin film was held at +1.0 V vs. Ag/AgCl/NaCl (3 M) for 120 s before recording the current response and switched to 0 V vs. Ag/AgCl/NaCl (3 M) at 0 s in the data. (f) Plot of current density *vs.* $t^{-0.5}$ extracted from (a)-(e). Red lines indicate the linear region for estimating apparent diffusivity.

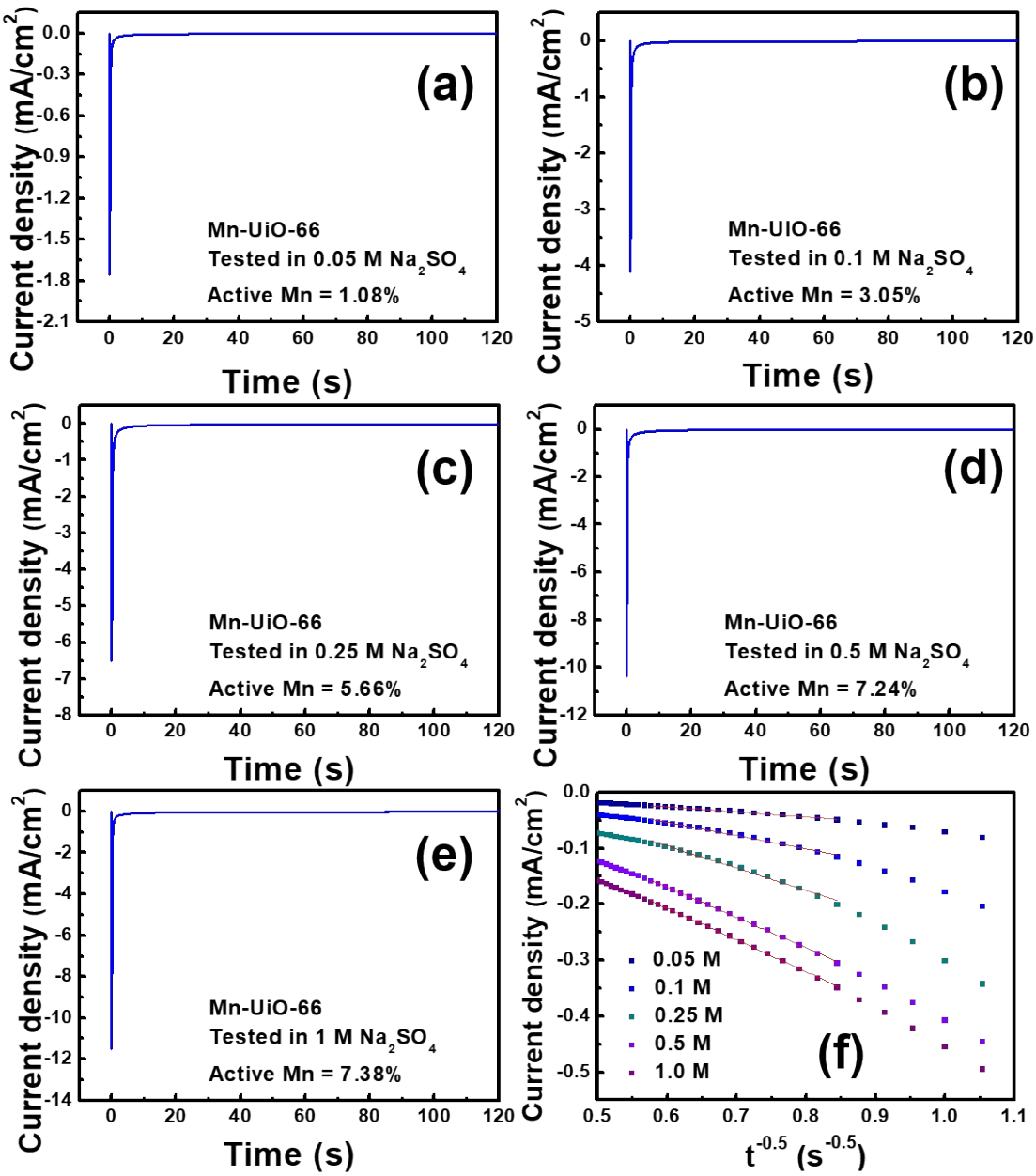

Figure S13. Chronoamperometric curves of Mn-UiO-66 thin films measured in (a) 0.05 M, (b) 0.1 M, (c) 0.25 M, (d) 0.5 M, and (e) 1 M Na_2SO_4 (aq). Each thin film was held at +1.0 V vs. Ag/AgCl/NaCl (3 M) for 120 s before recording the current response and switched to 0 V vs. Ag/AgCl/NaCl (3 M) at 0 s in the data. (f) Plot of current density *vs.* $t^{-0.5}$ extracted from (a)-(e). Red lines indicate the linear region for estimating apparent diffusivity.

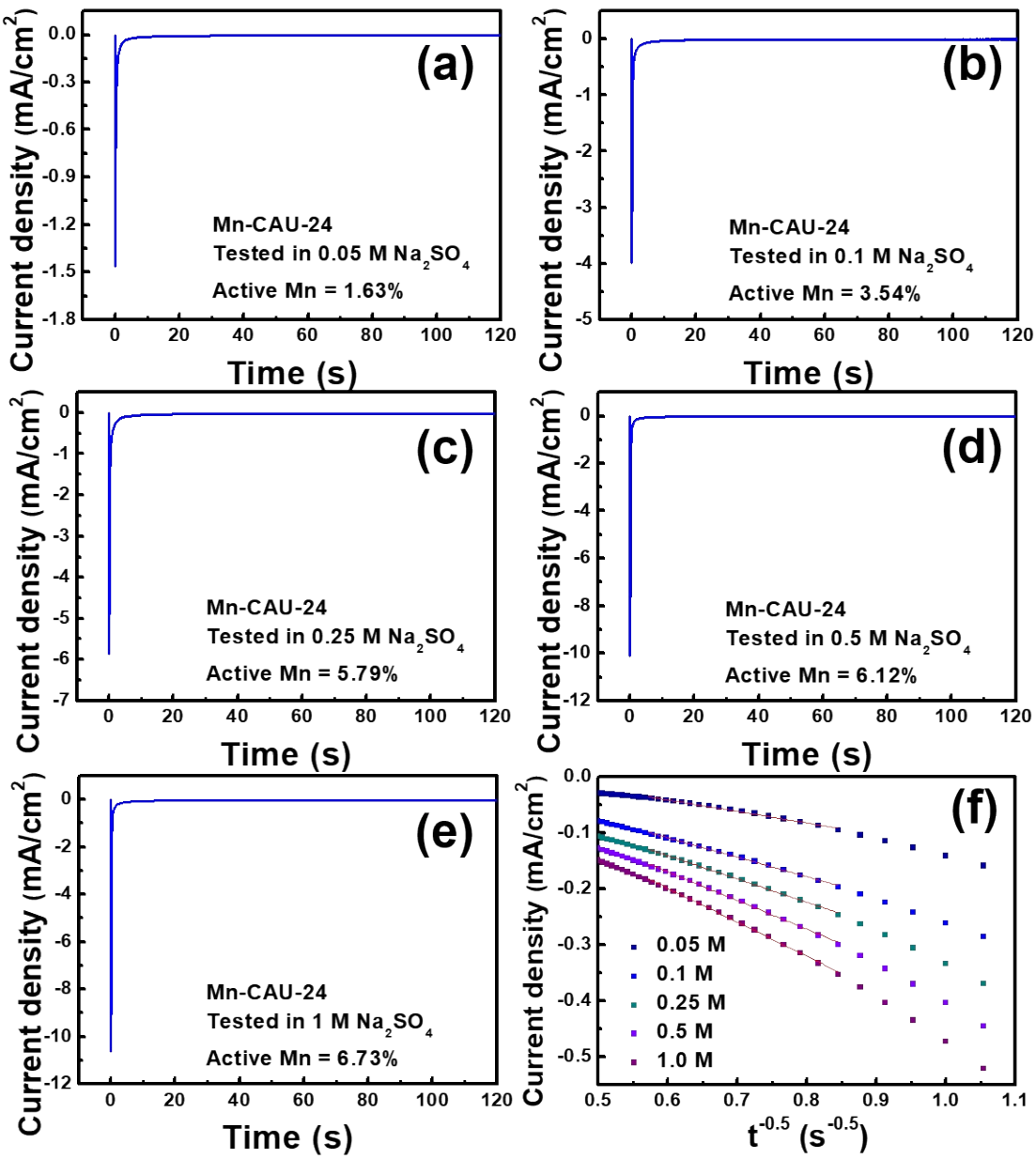

Figure S14. Chronoamperometric curves of Mn-CAU-24 thin films measured in (a) 0.05 M, (b) 0.1 M, (c) 0.25 M, (d) 0.5 M, and (e) 1 M Na_2SO_4 (aq). Each thin film was held at +1.0 V vs. Ag/AgCl/NaCl (3 M) for 120 s before recording the current response and switched to 0 V vs. Ag/AgCl/NaCl (3 M) at 0 s in the data. (f) Plot of current density *vs.* $t^{-0.5}$ extracted from (a)-(e). Red lines indicate the linear region for estimating apparent diffusivity.

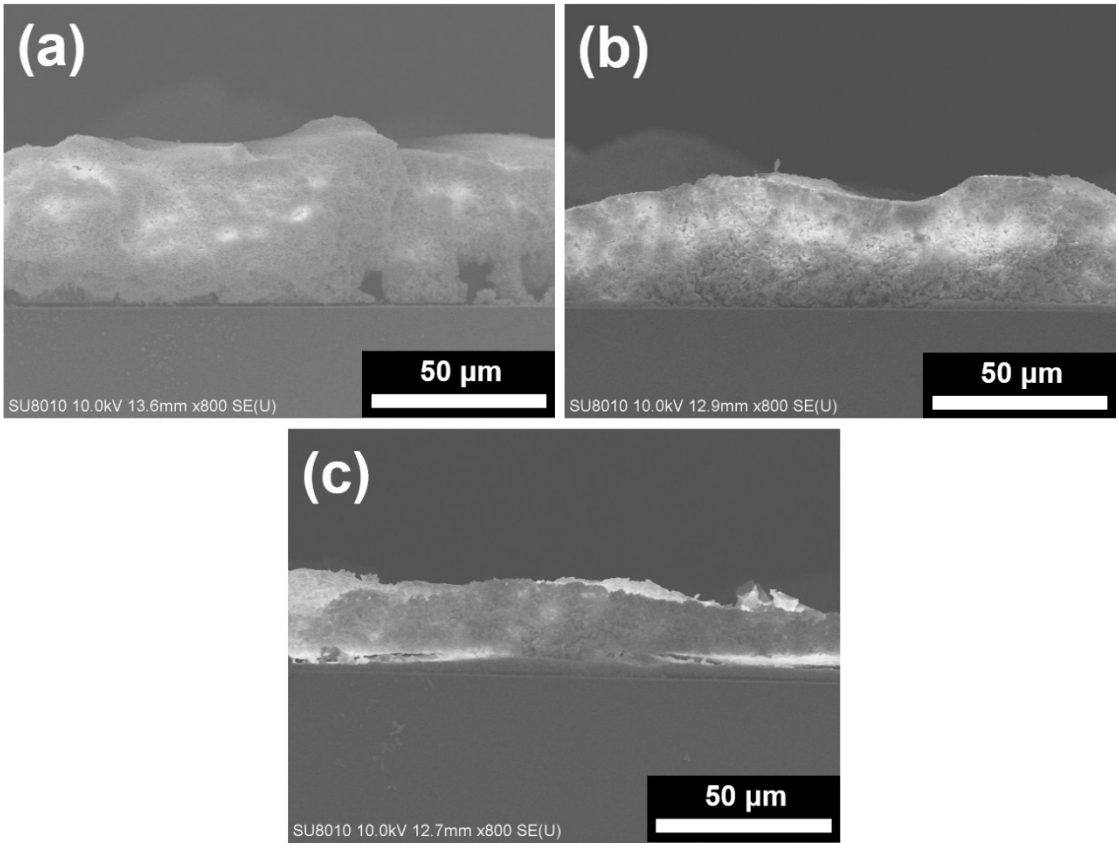

Figure S15. Cross-sectional SEM images of (a) Mn-MOF-808, (b) Mn-UiO-66, and (c) Mn-CAU-24 thin films.

Table S3. Calculation of the Mn concentration in each Mn-decorated MOF. The volume of unit cell and number of nodes in each unit cell were obtained from the reported crystal structures of these Zr-MOFs, and the Mn loading per node was obtained from ICP-OES data.

Material	Volume of unit cell (m^3)	Zr_6 nodes per unit cell	Mn per Zr_6 node	Concentration of Mn (mol/m^3)
Mn-MOF-808	4.32×10^{-26}	15.25	1.66	974
Mn-UiO-66	8.93×10^{-27}	4	0.91	677
Mn-CAU-24	7.89×10^{-27}	2	1.12	472

Table S4. Apparent diffusivity calculated from the linear regions shown in Figure S12(f), S13(f), and S14(f). These values are also plotted in Figure 8(b) of the main text.

Thin film / Concentration of electrolyte	0.05 M	0.1 M	0.25 M	0.5 M	1.0 M
Mn-MOF-808	9.5×10^{-11}	4.9×10^{-10}	6.2×10^{-10}	8.4×10^{-10}	9.8×10^{-10}
Mn-UiO-66	6.2×10^{-12}	4.1×10^{-11}	1.2×10^{-10}	2.2×10^{-10}	2.4×10^{-10}
Mn-CAU-24	6.4×10^{-11}	1.8×10^{-10}	2.6×10^{-10}	4.0×10^{-10}	5.1×10^{-10}

The values of D_{app} shown in Figure 8(b) (as well as in Figure S16(a) and Table S4) were estimated by using the concentrations of manganese sites presented in the crystal structures of these MOFs, which directly reflect the redox-hopping process within the MOF crystals. On the other hand, by using the manganese loadings in per square centimetres of the thin films and the average film thicknesses from the cross-sectional SEM images reported in the main text, the concentrations of manganese sites within the entire thin films normalized by the volumes including the interparticle space were calculated as 358 mol/m^3, 248 mol/m^3, and 324 mol/m^3 for Mn-MOF-808 thin film, Mn-UiO-66 thin film, and Mn-CAU-24 thin film, respectively. These values are a bit lower than those estimated from the crystal structures listed in the main text and Table S3. Values of D_{app} calculated by using these C values estimated from the average film thicknesses are plotted in Figure S16(b). It can be seen that since both the Mn-MOF-808 thin film and Mn-UiO-66 thin film have more interparticle volumes compared to the Mn-CAU-24 thin film, their C values are more significantly reduced when all the interparticle space is taken into account, which results in almost one order of magnitude higher D_{app} for both Mn-MOF-808 and Mn-UiO-66 compared to those calculated based on the C values from crystal structures. But such differences are not that obvious for the Mn-CAU-24 thin film, which is relatively densely packed. These results indicate that the values of D_{app} for MOF thin films may be different when different approaches are used to calculate the concentrations of the redox-active sites. However, both the results in Figure S16(a) and Figure S16(b) still show almost the same trend – The D_{app} increases significantly with increasing concentration of electrolyte in the low-concentration range, and it tends to be unchanged when the concentration of electrolyte is higher than 0.5 M.

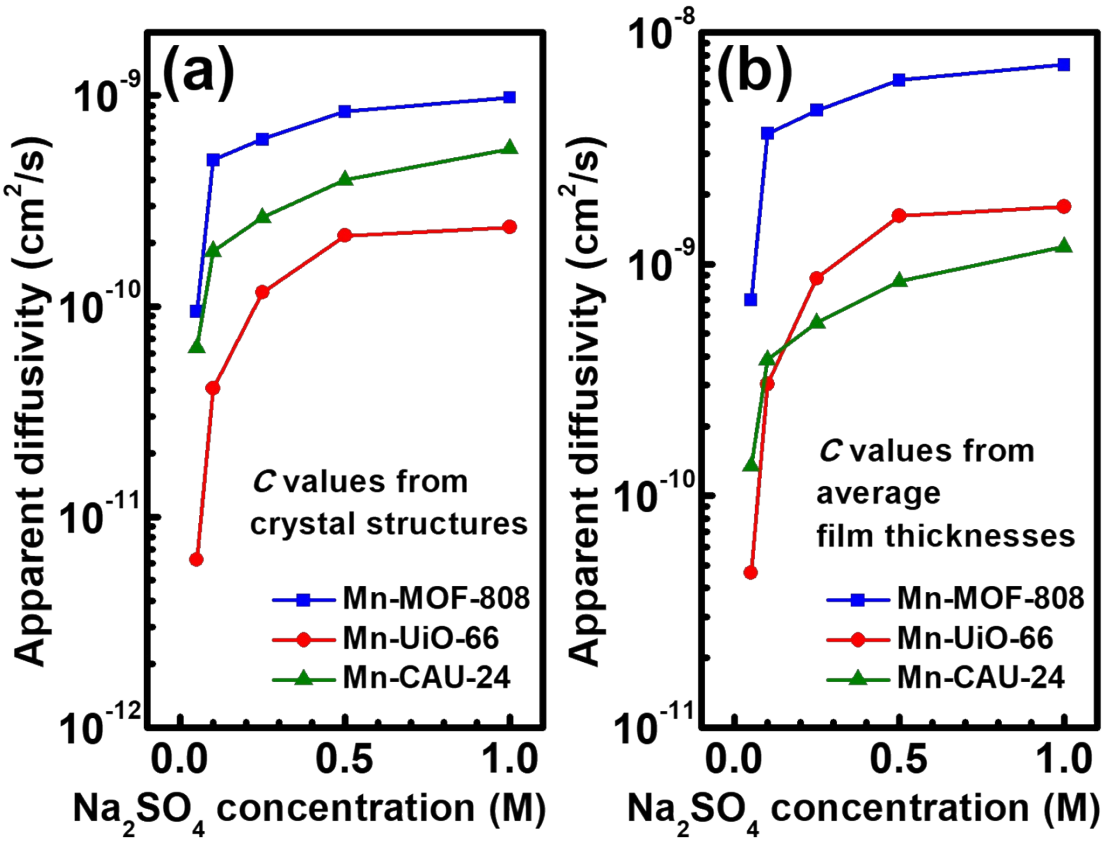

Figure S16. Values of apparent diffusivity of the Mn-decorated Zr-MOF thin films measured in various concentrations of electrolyte, calculated by using (a) the concentrations of manganese sites from crystal structures and (b) the concentrations of manganese sites from average film thicknesses. Figure S16(a) is also shown in the main text as Figure 8(b).

References:

1. B. Villoria-del-Álamo, S. Rojas-Buzo, P. García-García and A. Corma, *Chem. Eur. J.*, 2021, **27**, 4588-4598.
2. Y. Han, M. Liu, K. Li, Y. Zuo, Y. Wei, S. Xu, G. Zhang, C. Song, Z. Zhang and X. Guo, *CrystEngComm*, 2015, **17**, 6434-6440.
3. M. Lammert, H. Reinsch, C. A. Murray, M. T. Wharmby, H. Terraschke and N. Stock, *Dalton Trans.*, 2016, **45**, 18822-18826.
4. G. C. Shearer, S. Chavan, J. Ethiraj, J. G. Vitillo, S. Svelle, U. Olsbye, C. Lamberti, S. Bordiga and K. P. Lillerud, *Chem. Mater.*, 2014, **26**, 4068-4071.